Available online at www.sciencedirect.com

ScienceDirect

Journal of Magnesium and Alloys 12 (2024) 980–996

www.elsevier.com/locate/jma

Full Length Article

Grain refinement of Mg-Ca alloys by native MgO particles

Shihao Wang [a,b,c,*], Yun Wang [c], Quentin M. Ramasse [a,b], Zhongyun Fan [c]

[a] SuperSTEM Laboratory, SciTech Daresbury Campus, Daresbury WA4 4AD, UK
[b] School of Chemical and Process Engineering, University of Leeds, Leeds LS2 9JT, UK
[c] BCAST, Brunel University London, Uxbridge, Middlesex UB8 3PH, UK

Received 15 January 2024; received in revised form 7 March 2024; accepted 7 March 2024
Available online 22 March 2024

Abstract

In Mg-Ca alloys the grain refining mechanism, in particular regarding the role of nucleant substrates, remains the object of debates. Although native MgO is being recognised as a nucleating substrate accounting for grain refinement of Mg alloys, the possible interactions of MgO with alloying elements that may alter the nucleation potency have not been elucidated yet. Herein, we design casting experiments of Mg-xCa alloys varied qualitatively in number density of native MgO, which are then comprehensively studied by advanced electron microscopy. The results show that grain refinement is enhanced as the particle number density of MgO increases. The native MgO particles are modified by interfacial layers due to the co-segregation of Ca and N solute atoms at the MgO/Mg interface. Using aberration-corrected scanning transmission electron microscopy and electron energy loss spectroscopy, we reveal the nature of these Ca/N interfacial layers at the atomic scale. Irrespective of the crystallographic termination of MgO, Ca and N co-segregate at the MgO/Mg interface and occupy Mg and O sites, respectively, forming an interfacial structure of a few atomic layers. The interfacial structure is slightly expanded, less ordered and defective compared to the MgO matrix due to compositional deviations, whereby the MgO substrate is altered as a poorer template to nucleate Mg solid. Upon solidification in a TP-1 mould, the impotent MgO particles account for the grain refining mechanism, where they are suggested to participate into nucleation and grain initiation processes in an explosive manner. This work not only reveals the atomic engineering of a substrate through interfacial segregation but also demonstrates the effectiveness of a strategy whereby native MgO particles can be harnessed for grain refinement in Mg-Ca alloys.

Keywords: Mg-Ca alloy; Grain refinement; MgO; Interfacial segregation; STEM/EELS; Solidification.

1. Introduction

The unique physical and chemical properties of magnesium (Mg) have promoted a fast expansion of applications in fields of transportation, 3C and biological industries [1,2]. Its outstanding specific strength makes it one of the engineering material candidates to help and meet the ambitious 'net-zero' goals. In terms of manufacturing, casting is the most cost-efficient process for Near-Net-Shape magnesium products, accounting for 98.5% of structural applications of magnesium [3], where grain refinement is essential to improve the casting integrity and mechanical properties. Chemical inoculation through external addition to the melt is the traditional practice for grain refinement [4–6]. The mechanism of grain refinement lies in enhancing nucleation and grain initiation while impeding the heat from grain growth, which determines that nucleants and solutes are essential factors affecting grain refinement [4,7,8].

Microalloying offers Mg alloys different physical properties. Calcium (Ca) is one of the important alloying elements for magnesium alloys. Its addition underpins strategies for the enhancement of creep resistance, corrosion resistance, mechanical strength, biocompatibility, and grain refinement of Mg-Ca alloys [9–12]. The grain refining mechanism of Mg-Ca alloys involves the profound growth restriction effect of

* Corresponding author at: SuperSTEM Laboratory, SciTech Daresbury Campus, Daresbury WA4 4AD, UK.
E-mail address: swang@superstem.org (S. Wang).

https://doi.org/10.1016/j.jma.2024.03.009

Ca, as well as the specific nucleant sites in the melt, although these remain unknown [5,11]. The nature of the nucleating particles is a general scientific issue for eutectic metallic alloy systems. Some recent work indicated that native MgO might be a nucleating candidate in Mg-Ca alloys, in which CaO was added as an alternative to Ca [13–15]. It was proposed that the reduction product MgO serves as the nucleating substrate, while Ca solute released back to the melt provides sufficient growth restrictions [13–17]. The work by Ali *et al.* indicated that some CaO particles could survive after reaction and act as nucleation sites [18], as evidenced by the identification of CaO at the centre of α-Mg grains, along with the good potency predicted by the crystallographic matching calculation. In Mg-Ca alloys without the addition of CaO, our previous work proposed that the native MgO particles of good dispersion after high shear melt conditioning (HSMC) treatment account for the grain refinement [19,20]. However, more research on the mechanisms at play is required to establish a full understanding of grain refinement in these systems and of the interplay between the native MgO and the Ca solutes.

MgO particles on their own were found to refine the as-cast microstructure of different Mg alloys, and this was indeed once a proposed mechanism for the refinement of Mg-Al alloys treated by superheating [21]. High-resolution transmission electron microscopy (HRTEM) recently revealed that the MgO/Mg interface adopts a well-defined orientation relationship [22], providing clues for why MgO particles can act as nucleating substrates for the Mg solid. In practice and as a consequence of these findings, it was shown that native MgO agglomerates (oxide films) that possess a potentially high number density of nanoparticles could be exploited through HSMC for grain refinement [19,20,22,23]. In addition to '*in-situ*' MgO particles [22–28], external MgO addition [29,30] was also reported as a means to reduce the grain size of several types of Mg alloys after solidification. This work aims to verify conclusively the role of native MgO in grain refinement of Mg-Ca alloys, by evaluating the grain size of Mg-Ca alloys commensurate with the number density of MgO particles.

The effect of solutes on grain refinement is not limited to providing growth restriction. Extra effects may result from: *i*) the chemical reactions with other solutes or inoculants [31–35] and *ii*) interfacial segregation [20,36–44]. The possible changes in nucleant particles (potency, number density, size and size distribution) and solute concentrations alter the solidification behaviour and final microstructure. To boost native MgO particles for refining Mg-Ca cast alloys, it becomes critical to understand the interactions between MgO and Ca, which have not been fully understood yet [19,20,45–47]. It is well-established that Ca segregation on the MgO {001} surface is energetically favourable [45,46]. Our previous experimental study suggested that the Ca segregation behaviour at the MgO/Mg interface takes place through the formation of Ca-rich atomic layers with an lattice structure resembling the MgO matrix [20]. In contrast, Peng *et al.* interpreted the Ca-segregation layers as Mg_2Ca 2DC layers [19,47]. The atomic structure of Ca-segregation layers therefore remains ambiguous. More efforts are required to elucidate the interaction between MgO and Ca in Mg-Ca alloys, which is a critical step for the clarification of grain refining mechanism, and towards practical applications of native MgO to Mg-Ca alloy series, as well as further extensions to other Mg alloys.

In this work, we first present experimental evidence for the grain refinement of Mg-Ca alloys by native MgO particles. After casting into a TP-1 mould, three sets of Mg-xCa alloys, with qualitatively different number densities of native MgO particles, are evaluated by grain size measurements. The structural and chemical nature of Ca segregation at the MgO/Mg interfaces is then extensively studied at the atomic scale by state-of-the-art scanning transmission electron microscopy (STEM) and electron energy loss spectroscopy (EELS). Atomic segregation layers containing Ca and N are identified, with the lattice structure slightly expanded and less ordered compared to the MgO matrix. Based on the experimental results, we attribute the grain refinement mechanism of Mg-Ca alloys after HSMC to the depressed nucleation potency, enhanced dispersity of native MgO particles, and sufficient growth restriction for columnar to equiaxed transition. This work sheds light on how to harness native MgO particles in Mg alloys.

2. Experimental methods

Commercial purity magnesium (CP Mg, > 99.9%, in wt.% unless otherwise specified) and pure calcium (99.9%) were used as the raw materials, which were melted in the unit comprising an electric resistance furnace, a steel liner, a steel tube to deliver the mixture gas of 99.5 vol.% N_2 and 0.5 vol.% SF_6, and a K-type thermocouple.

As illustrated in Fig. 1, three sets of casting experiments were carried out to qualitatively change the number density of native MgO in Mg-xCa alloys (x = 0.05, 0.1, 0.3, 0.5, 0.7, 1%). For experiment set one (Fig. 1a), CP Mg ingot was initially melted at 700°C in a steel crucible protected by the mixture gas. A certain content of pure Ca granules was added to make a specific Mg-xCa melt. It was held isothermally for 30 min, during when manual stirrings were applied every 5 min to facilitate homogeneity. After that the melt was cooled down to 680°C, finally stirred and poured in to a 350°C pre-heated TP-1 mould, which was transferred to a cooling unit that provided a cooling rate of 3.5 $K{\cdot}s^{-1}$ at the cross section 38mm from the bottom. These cast ingots were denoted as Mg-xCa, in which 'x' refers to the weight fraction of Ca.

As based on set one, an additional HSMC treatment was applied to the Mg-xCa melts in experiment set two (Fig. 1b) after homogeneity, aiming to disperse native MgO particles/films, thus to increase their effective number density. According to the previous work [23], the estimated particle number density is $10^{14}/cm^3$ without HSMC, while it is increased to $10^{17}/cm^3$ after HSMC. The HSMC treatment was delivered to the melts at 700°C by a rotor-stator mixer, which was positioned 40 mm beneath the melt surface and operated at a speed of 4000 rpm for 5 minutes. The solidified TP-1 samples in set two are therefore named with a '-HSMC' suffix, *i.e.*, Mg-xCa-HSMC.

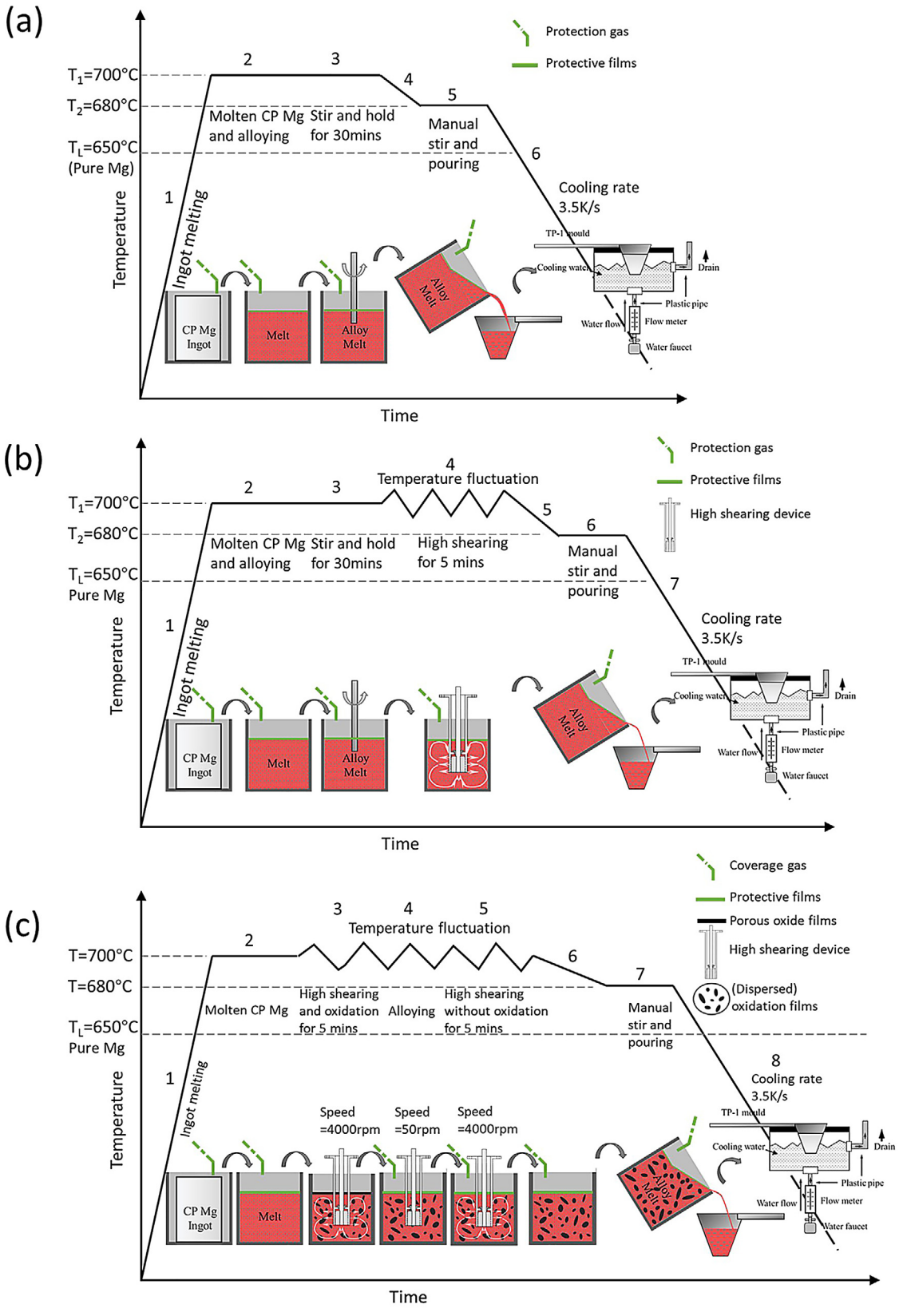

Fig. 1. Flow diagrams showing the casting procedures of (a) TP-1 test (Mg-xCa); (b) TP-1 test with prior HSMC treatment (Mg-xCa-HSMC); and (c) TP-1 test with controlled oxidation and HSMC treatment (Mg-xCa-HSO).

In experiment set three (Fig. 1c), since Ca addition increases the melt's oxidation resistance, HSMC with controlled oxidation (HSO) was applied to the CP Mg melt prior to alloying. Before inserting the HSMC mixer, we removed the protection gas and scraped the melt surface film to expose the melt to the atmosphere. This allowed melt oxidation during HSMC treatment. The HSMC parameters remained the same as 4000 rpm and 40 mm deep into the melt at 700°C. During this period, oxidation products appeared on the melt surface, and they were pushed into the melt, by which newly generated oxides can be dispersed by the mixer and introduced into the melt. Afterwards, the CP Mg melt was recovered by protection gas and the mixer speed was decreased down to 50 rpm for the addition of Ca. This was followed by another 5-minutes HSMC treatment to ensure the dispersion of native MgO particles and homogeneity of Ca dissolution. The Mg-xCa melt with qualitatively more oxides in good dispersity then was cooled down to 680°C, manually stirred and cast into the TP-1 mould. The cast ingots in experiment set three were labelled as Mg-xCa-HSO.

The solidification structure and grain size of Mg-xCa alloys were assessed on the sectioned part 38 mm from the bottom of the solidified TP-1 ingots. The central area of the transverse section was etched for precise grain size measurement, while the longitudinal section was for evaluating the macroscopic grain structure. The polished specimens were etched in an acetic-picral solution that contains 10 ml acetic acid, 4.2 g picric acid, 10 ml H_2O and 140 ml ethanol. An Epson image scanner and a Zeiss optical microscope (OM) were used for optical macrography and micrography, respectively. The quantification of the columnar grain width and equiaxed grain size of the samples was conducted according to the mean linear intercept method (ASTM E112-10).

A Prefil®-Footprinter unit was applied for melt filtration to concentrate and collect the inclusion particles from Mg-0.5Ca for electron microscopy characterisation. 1.2 kg Mg-0.5Ca melt was transferred into a pre-heated crucible fixed in an isolated chamber, followed by argon introduction to press the melt through a filter attached at the bottom of the crucible. The solidified ingot above the filter contains concentrated native MgO and other possible impurity inclusions.

The as-cast microstructure and MgO films/oxides were characterised by a Carl Zeiss Crossbeam 340 SEM equipped with an energy-dispersive X-ray spectroscopy (EDS) detector. Conventional TEM characterisation of the native MgO films/oxides was conducted on a JEOL JEM-2100F microscope at an accelerating voltage of 200 kV. Extensive characterisation of MgO/Mg interfaces was carried out on an aberration-corrected Nion UltraSTEM100 instrument at the SuperSTEM laboratory. The microscope possesses an optimum probe optics configuration with a 31 mrad convergence semi-angle and a 1 Å probe size at 100 kV, allowing atomic-resolution imaging and spectroscopy. The collection angles for high angle annular dark-field (HAADF) STEM images are 89–195 mrad, while they are 52–89 mrad for the medium angle annular dark-field (MAADF) detector. A Gatan Enfina electron energy loss spectrometer (EELS) was used for chemical analysis. When the probe scans over an area of interest, an EELS spectrum was acquired at each pixel to form an EELS spectrum image (EELS SI). Noise reduction of EELS SI data was conducted by principal component analysis (PCA), as implemented in the HREM Research MSA plugin for Digital Micrograph [48].

3. Results

3.1. Effect of Ca and HSMC on grain size

The strong growth restriction effect of Ca in its use for grain refinement of Mg alloys [11] is illustrated by the evolution of the grain structure as a function of Ca concentration (Fig. 2), whereby the grain structure is getting further equiaxed and refined with Ca addition. It is seen that coarse columnar grains dominate at low Ca concentrations, which gradually diminish when the Ca addition increases from 0.05% to 0.3%. In Mg-0.3Ca, the grains appear equiaxed in the central area, while they are still columnar near the edge. The addition of 0.5Ca achieves a complete columnar-to-equiaxed transition (CET) across the Mg-0.5Ca ingot with different cooling conditions, associated with a significant grain size reduction. Afterwards, subsequent Ca additions (0.7% to 1%) reduce moderately the average grain size (AGS). The grain size evolution observed here agrees with previous work suggesting that grain size is inversely proportional to the solute content that provides growth restriction during solidification [11].

High shear melt conditioning has been shown as an effective physical method to produce a fine as-cast microstructure of Mg and Al alloys through *i*) the dispersion of either native or exogenous nucleants; *ii*) a homogeneous temperature profile; *iii*) a homogeneous composition profile; *iv*) physically promoted wetting [27,49,50]. Fig. 3 presents the grain structure of Mg-xCa alloys with HSMC treatment prior to casting. A similar evolution of grain size is seen as the Ca content varies, *i.e.*, initially, the grain structure is dramatically refined together with CET, while further Ca additions subsequently show relatively minor effects. The positive contribution from HSMC treatment is clearly seen by comparing to the results without HSMC in Fig. 2. Apparently, CET is advanced by the HMSC treatment as less Ca is required; a full CET occurs in Mg-0.3Ca-HSMC. Furthermore, at the same Ca concentration, the set with prior HSMC treatment has a smaller grain size than that without HSMC. The advanced CET and smaller grain size suggest that more particles are available and activated for grain initiation when HSMC is applied.

3.2. The native inclusions: MgO

Inclusions collected from Mg-0.5Ca melt (Mg-0.5Ca-prefil) were examined by electron microscopy. Among the collected native inclusions, two typical types of nanoparticle are found: one has a polyhedral shape (Fig. 4a) and the other has a cubic shape (Fig. 4b). The energy dispersive X-ray spectroscopy (EDS)

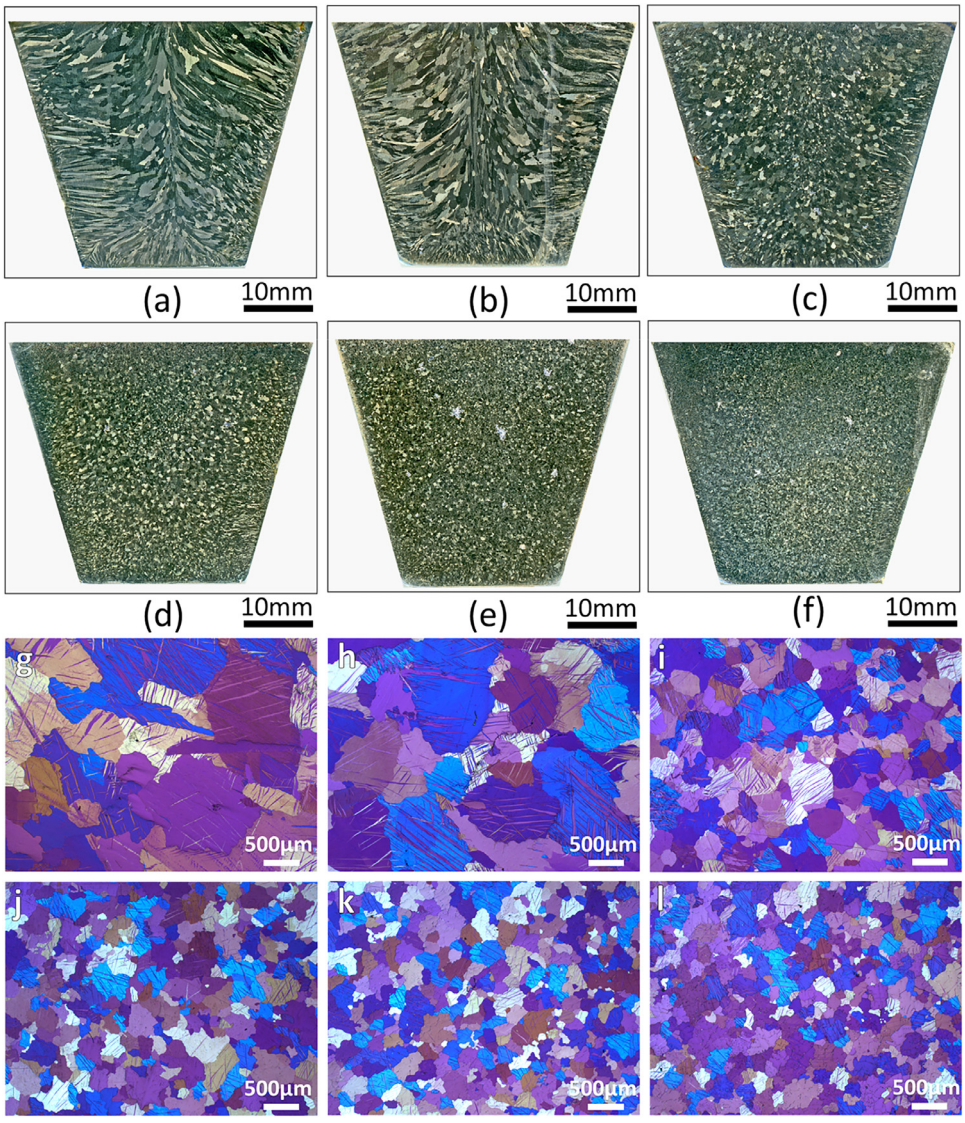

Fig. 2. The effect of Ca on grain refinement in Mg-Ca alloys without prior HSMC treatment. (a–f) Macro- and (g-l) micro-optical graphs showing the grain structures of (a, g) Mg-0.05Ca, (b, h) Mg-0.1Ca, (c, i) Mg-0.3Ca, (d, j) Mg-0.5Ca, (e, k) Mg-0.7Ca and (f, l) Mg-1Ca. Note that the micrographs are acquired on the transverse sections of the TP-1 ingot 38 mm from the bottom.

analysis suggests that they are mainly composed of Mg and O (Fig. 4c). These nanoparticles possess the same morphologies, sizes, and compositions as the MgO particles found in CP Mg and Mg-9Al in our previous work [24]. Given these combined observations, the native particles in Mg-0.5Ca-prefil can therefore be recognised as octahedral {111} MgO particles and cubic {100} MgO nanoparticles, respectively. The addition of 0.5% Ca negligibly affects their phase stability, sizes, and morphologies compared to the earlier study without any Ca. Systematic SEM analysis suggests that the predominant inclusions overall in the Mg-0.5Ca-prefil sample are MgO films/particles. Interestingly, a systematic, albeit weak Ca enrichment on the MgO is identified by EDS analysis (Fig. S1). A typical example in Fig. 4d shows the weak Ca K characteristic X-ray signals detected from both types of MgO particles, with intensities higher than any remaining Ca base signal in spectra acquired from the Mg matrix. The extra Ca K peaks are too weak to originate from Ca-rich phases. Similarly, the presence of CaO is less likely as suggested by the uniform contrast in the backscattered-electron images of both MgO films (Fig. S2). It is more likely that the detected Ca enrichment results from Ca segregation at/near the MgO particles.

The particulate oxide film consisting of {111} MgO particles was further characterised by bright-field (BF) TEM imaging and selected area electron diffraction (SAED) in Fig. 5. It is seen that discrete nanometre sized MgO particles are embedded in the Mg matrix, often clustering into agglomerates (Fig. 5a). Fig. 5b shows the corresponding SAED pattern, where indexing and interpretation of the characteristic diffraction ring patterns suggest that the oxide film consists of randomly oriented MgO particles. Consistently with the

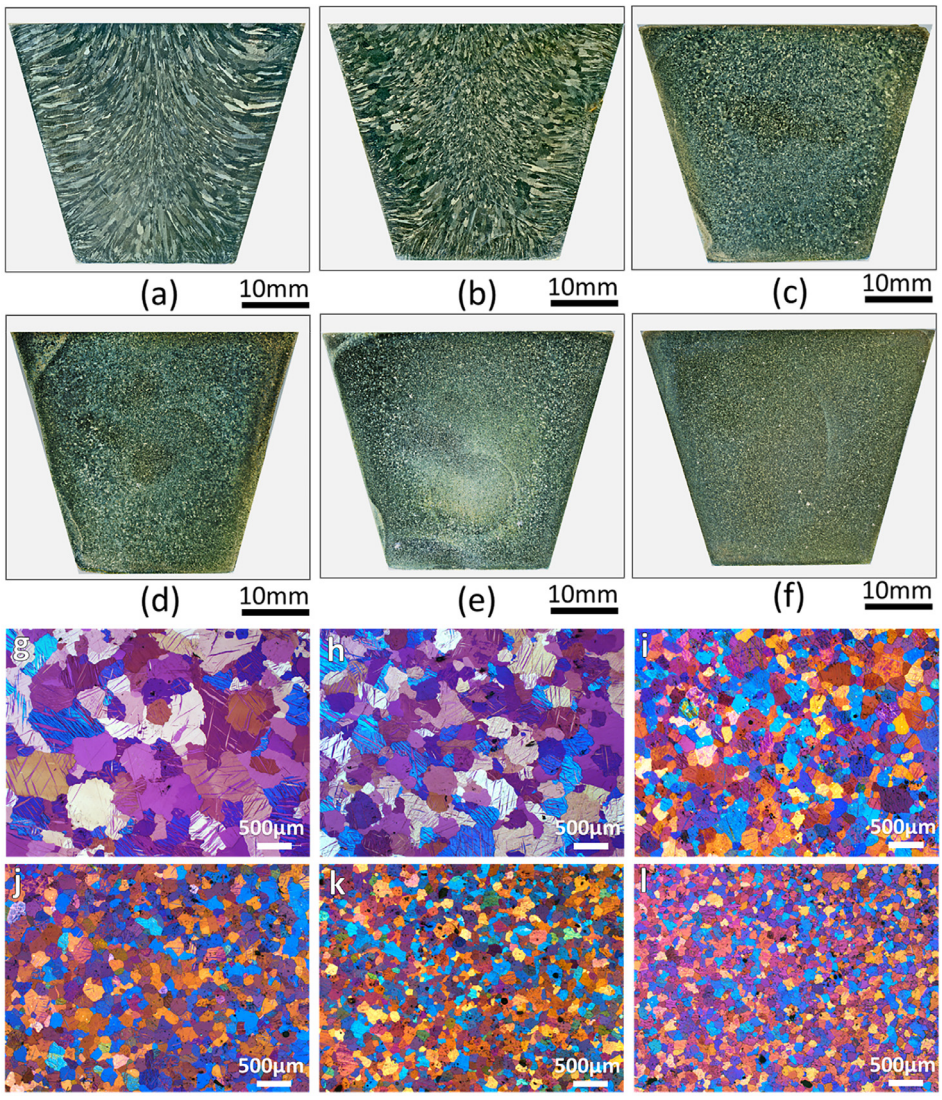

Fig. 3. The effect of Ca on grain refinement in Mg-Ca alloys with prior HSMC treatment. (a–f) Macro- and (g–l) micro-optical graphs showing the grain structures of (a, g) Mg-0.05Ca-HSMC, (b, h) Mg-0.1Ca-HSMC, (c, i) Mg-0.3Ca-HSMC, (d, j) Mg-0.5Ca-HSMC, (e, k) Mg-0.7Ca-HSMC and (f, l) Mg-1Ca-HSMC. Note that the micrographs are acquired on the transverse sections of the TP-1 ingot 38 mm from the bottom.

SEM analysis (Figs. 4, S1, 2), no other phases are identified from the SAED pattern, indicating that MgO is the predominant inclusion in the Mg-0.5Ca melt.

Although other non-metallic phases like Mg_3N_2, MgF_2, MgS are possible inclusions in the melt of Mg alloys, the predominant inclusions are oxides [51]. Moreover, recent experimental studies conclusively verified that, although this conflicts with their relative positions in Ellingham diagram [52], CaO dissolves in Mg-Ca alloy melts [14,15,17]. The present results further confirm that the detected particles in Mg-0.5Ca-prefil are MgO (Figs. 4 and 5).

3.3. Generating more oxides for grain refinement by HSO

Dispersed native MgO particles were proposed to contribute to the grain refinement of Mg alloys after HSMC [22]. This agrees with the fact that finer grains in Mg-1Ca-HSMC are frequently found in association with MgO clusters (Fig. S3d). To further verify the effect of MgO on grain refinement, the number density of MgO particles was qualitatively increased by controlled melt oxidation in experiment set three (Fig. 1c). As summarised in Figs. 6 and 7, the introduction of more MgO particles in Mg-xCa-HSO not only advances further the occurrence of CET but also achieves the finest grain sizes among the three sets, which is expected as more MgO has been introduced as nucleant particles into the melt (Figs. S3 and S4). With HSO treatment, the critical Ca content for CET falls to 0.1%. The AGS of Mg-1Ca drops from 163.7 ± 11.5 μm to 95.5 ± 4.7 μm when HSMC is applied, and it decreases further down to 61.4 ± 5.6 μm when HSO is implemented. The introduced MgO particles are distributed across the Mg matrix, with many of them engulfed within the grains rather than pushed to grain boundaries (Figs. S3g–i and S4g–i). The results, along with the comparison of plots showing the grain evolution of Mg-xCa, Mg-xCa-HSMC and Mg-xCa-HSO as a function of Ca content in Fig. 7, illustrate

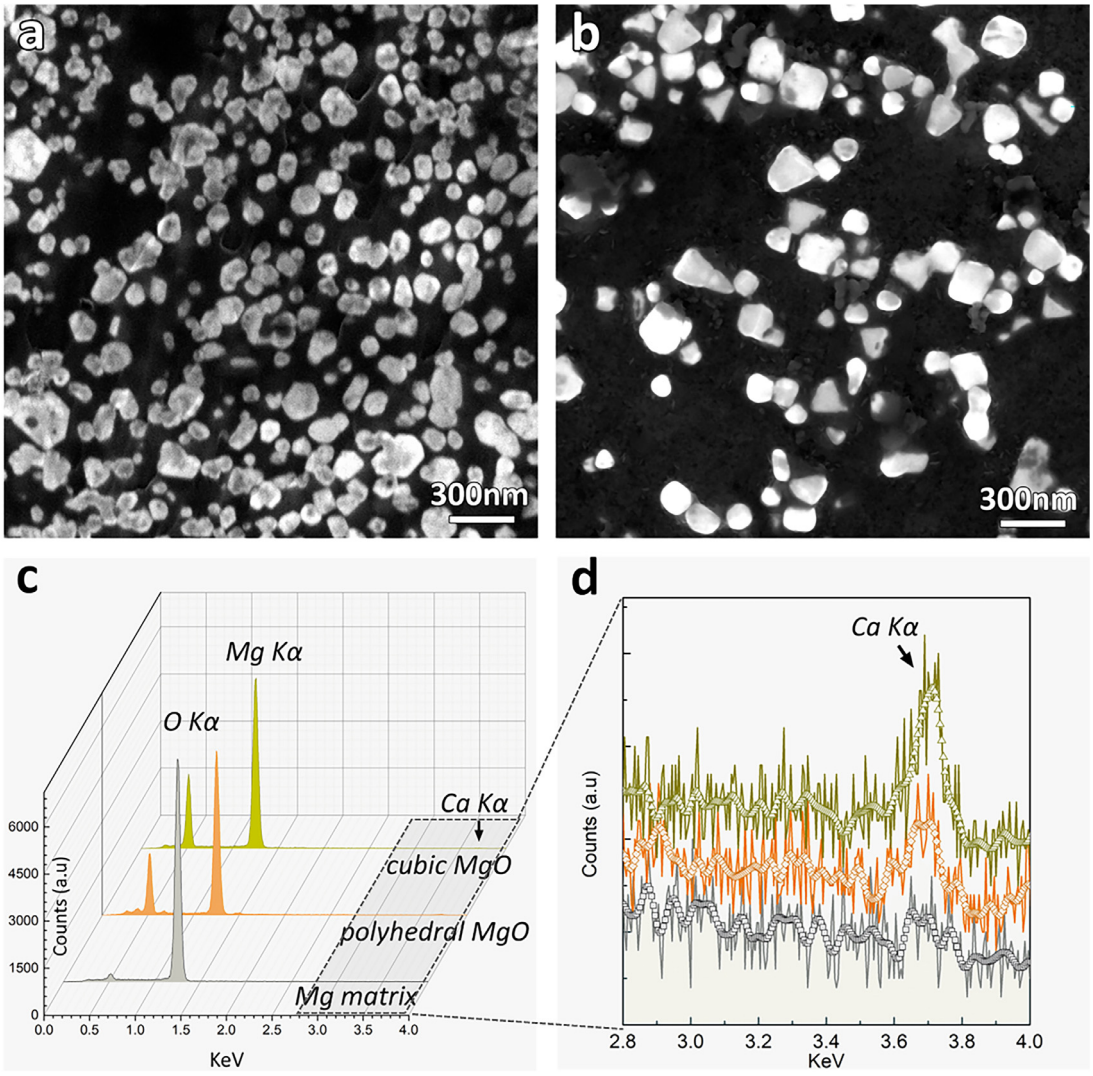

Fig. 4. Native MgO particles in Mg-0.5Ca-prefil. (a, b) Secondary electron (SE) SEM images of the octahedral MgO and cubic MgO particles, and (c, d) EDS spectra showing the extra Ca K peaks detected from MgO particles.

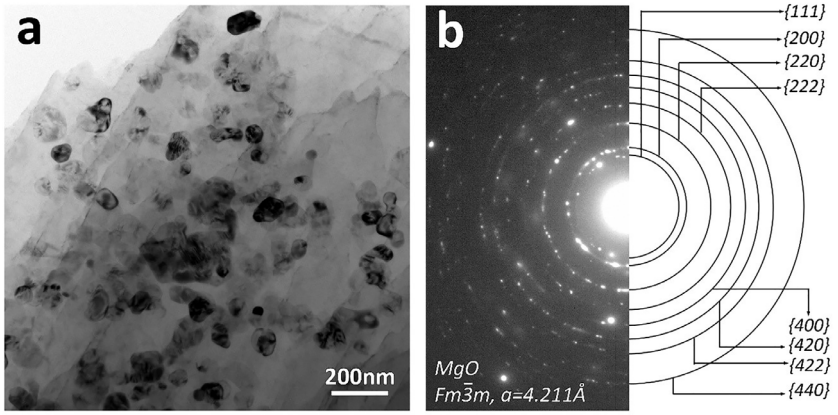

Fig. 5. (a) BF TEM image of MgO agglomerates in an oxide film and (b) the corresponding selected area electron diffraction pattern with index.

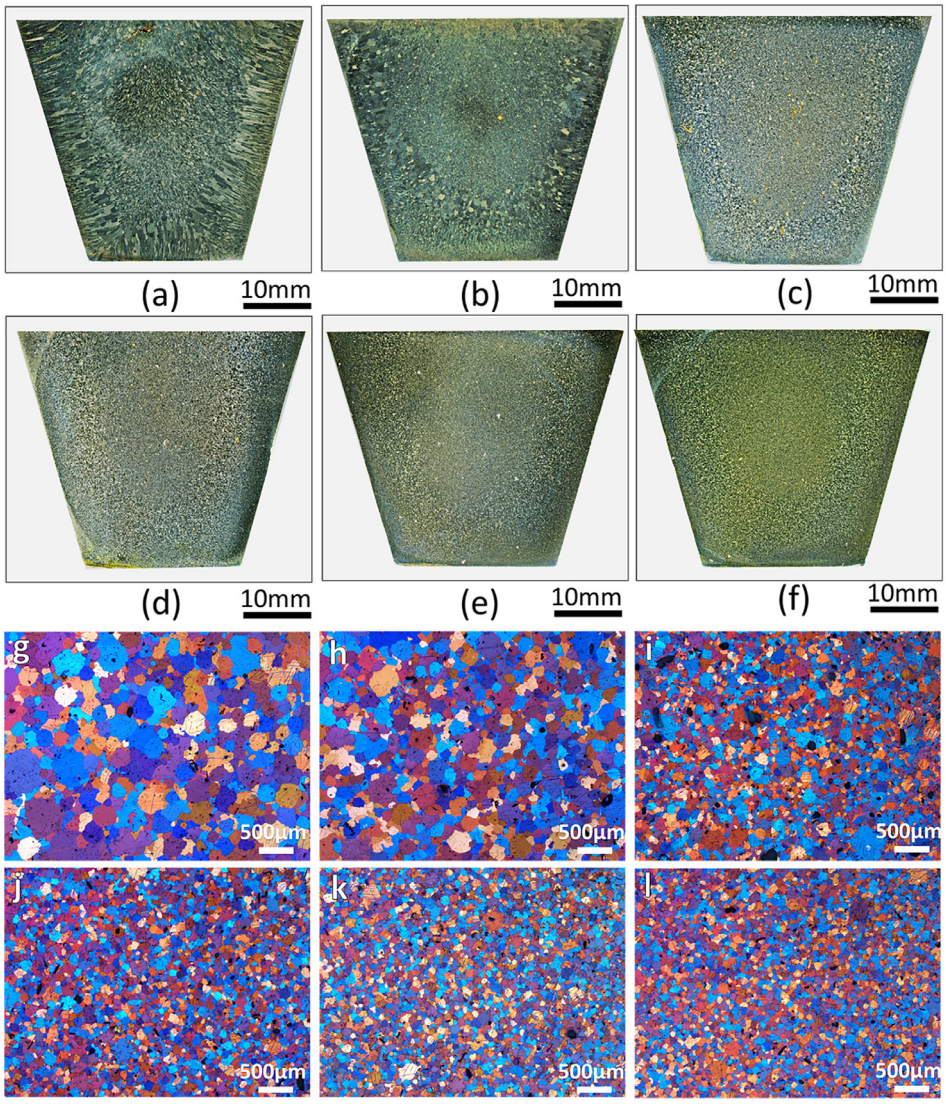

Fig. 6. The effect of Ca on grain refinement in Mg-Ca alloys with extra oxidation and HSMC treatment (HSO). Optical (a-f) macro- and (g-l) micrographs showing the grain structures of (a, g) Mg-0.05Ca-HSO, (b, h) Mg-0.1Ca-HSO, (c, i) Mg-0.3Ca-HSO, (d, j) Mg-0.5Ca-HSO, (e, k) Mg-0.7Ca-HSO and (f, l) Mg-1Ca-HSO. Note that the micrographs are acquired on the transverse sections of the TP-1 ingot 38 mm from the bottom.

clearly how well-dispersed MgO particles with a high number density contribute to a finer grain size and an advanced CET. It is therefore very likely that the MgO particles are the nucleating substrates for the Mg grains, especially given that in Mg-xCa melts MgO was confirmed as the overwhelmingly predominant inclusion type.

3.4. Elemental segregation of Ca and N at MgO/Mg interface

Since MgO remains the predominant type of particle inclusions in Mg-xCa alloys and given the observation of higher Ca content in their vicinity than within the Mg matrix, the nature of the Ca segregation must be established in terms of its structure and chemistry in order to understand any extra effects (other than growth restriction) it may have on solidification. Aberration-corrected STEM/EELS was used to further investigate the detected Ca enrichment on MgO particles down to the atomic scale. Since all grain-size plots in Fig. 7 have passed the inflection point at 0.5Ca and show relatively small changes afterwards, the addition of 0.5Ca represents a condition where both growth restriction and elemental segregation synergistically contribute to the grain refinement. Hence, the MgO/Mg interfaces in Mg-0.5Ca alloy after pressurised melt filtration were chosen as representatives for segregation analysis. Considering the crystal structure of MgO and the morphological feature of both MgO particle types, we adopted $<011>_{MgO}$ or $<211>_{MgO}$ zone axes to analyse the edge-on MgO/Mg interfaces for {111} MgO particles, while $<001>_{MgO}$ or $<011>_{MgO}$ directions for {100} MgO particles.

Fig. 8 presents representative HAADF STEM images of a {111} MgO (Fig. 8a, b) and a {100} MgO particle (Fig. 8c, d) observed from $[01\text{-}1]_{MgO}$ and $[001]_{MgO}$ directions, respectively. It is seen that the MgO particles, regardless of the crystallographic terminations, are decorated by interfacial segre-

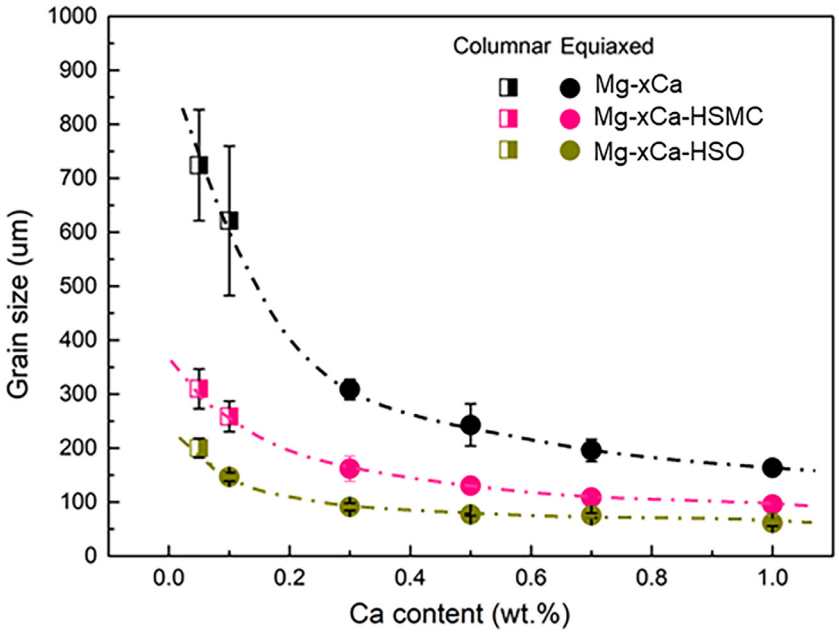

Fig. 7. Comparison of the average grain size or average columnar width of Mg-xCa, Mg-xCa-HSMC and Mg-xCa-HSO alloys as a function of Ca content.

gation of a few atomic layers in thickness, as suggested by the variations in contrast profiles across all MgO/Mg interfaces. Since featureless MgO/Mg interfaces with uniform contrast were observed in commercial purity Mg [24], the formation of interfacial layers in Mg-0.5Ca appears to directly correlate with the addition of Ca solutes to the melt. The HAADF signal is proportional to the nth power (n = 1.5–2) of the atomic number Z, and thus often described as 'Z contrast'. Given that the thickness of the specimen was verified to be even across the interfaces using low-loss EELS measurements [53], the change in contrast observed here suggests a chemical variation across the interfacial layers.

The compositional variations were verified by EELS analysis across the MgO/Mg interface. Fig. 9a shows an HAADF STEM image of a $\{111\}_{MgO}$/Mg interface, acquired under a $<211>_{MgO}$ projection. The core-loss EELS spectra extracted from the corresponding colour-filled boxes reveal prominent Ca $L_{2,3}$ and N K core-loss signal in the spectrum extracted from the interfacial layers, which is absent on either side of the interface. Ca and N are also seen to be concentrated in the interfacial layers, as shown in the EELS elemental maps (Fig. 9e–h). This confirms the co-segregation of Ca and N at the MgO/Mg interface. The elemental distribution of Ca and N coincides with the depletions in Mg and O and with the lower contrast observed in HAADF at the interfacial layers. An offset between the maxima in the Ca and N integrated signal is observed, as highlighted by the solid and dashed lines on Fig. 9g, respectively. This suggests a lower N content towards the outermost layers of the interfacial structure. As opposed to the relatively lower HAADF intensity compared to the MgO matrix (Fig. 9c), the Ca/N co-segregation layers appear brighter in the MAADF STEM image (Fig. 9d). The MAADF image formation intensity is complex and can be described as containing a component of strain contrast from the low-angle-scattered electrons [54]. The abrupt changes of MAADF contrast point out that the local periodicity and crystal structure get disrupted going from the MgO matrix to the Ca/N-rich interfacial layers.

3.5. Atomic structure of the Ca/N co-segregation layers

Fig. 10a, b show HAADF STEM images of the $\{111\}_{MgO}$/Mg interfaces along $[011]_{MgO}$ and $[112]_{MgO}$ directions, respectively. Upon closer inspection, interfacial segregation layers comprising three to four atomic layers of lower brightness than the MgO matrix are distinguishable (Fig. 10a–d). Along the $[011]_{MgO}$ projection, the atomic pattern of the interfacial segregation layers is nearly identical to that of the MgO matrix, with a minor increase of the interplanar/interatomic spacings (Fig. 10c). The measured expansion is 0.028 nm along the $<112>_{MgO}$ direction ('P1' in Fig. 10a) and 0.025 nm along the normal direction of $(11\text{-}1)_{MgO}$ ('P2' in Fig. 10b), accounting for a ~10% expansion of the lattice constant. As atomic columns become more densely spaced when observed under the $[112]_{MgO}$ zone axis (Fig. 10b), the atomic structure of the interfacial layers becomes harder to resolve. This also points to some level of deviation from the atomic structure of MgO, as the last lattice plane of the MgO particle remain resolvable. As chemically revealed by the EELS elemental maps in Fig. 10d, such local structural deviations are related to the local compositional deviations. These maps reveal that the first two interfacial layers, which display the same atomic pattern but with lower intensity than the MgO 'bulk', coincide with the highest Ca and N signal while being depleted in Mg and O. Similarly, Fig. S6 shows the elemental distribution across the interface projected along $[112]_{MgO}$. The very tight atomic spacings and the

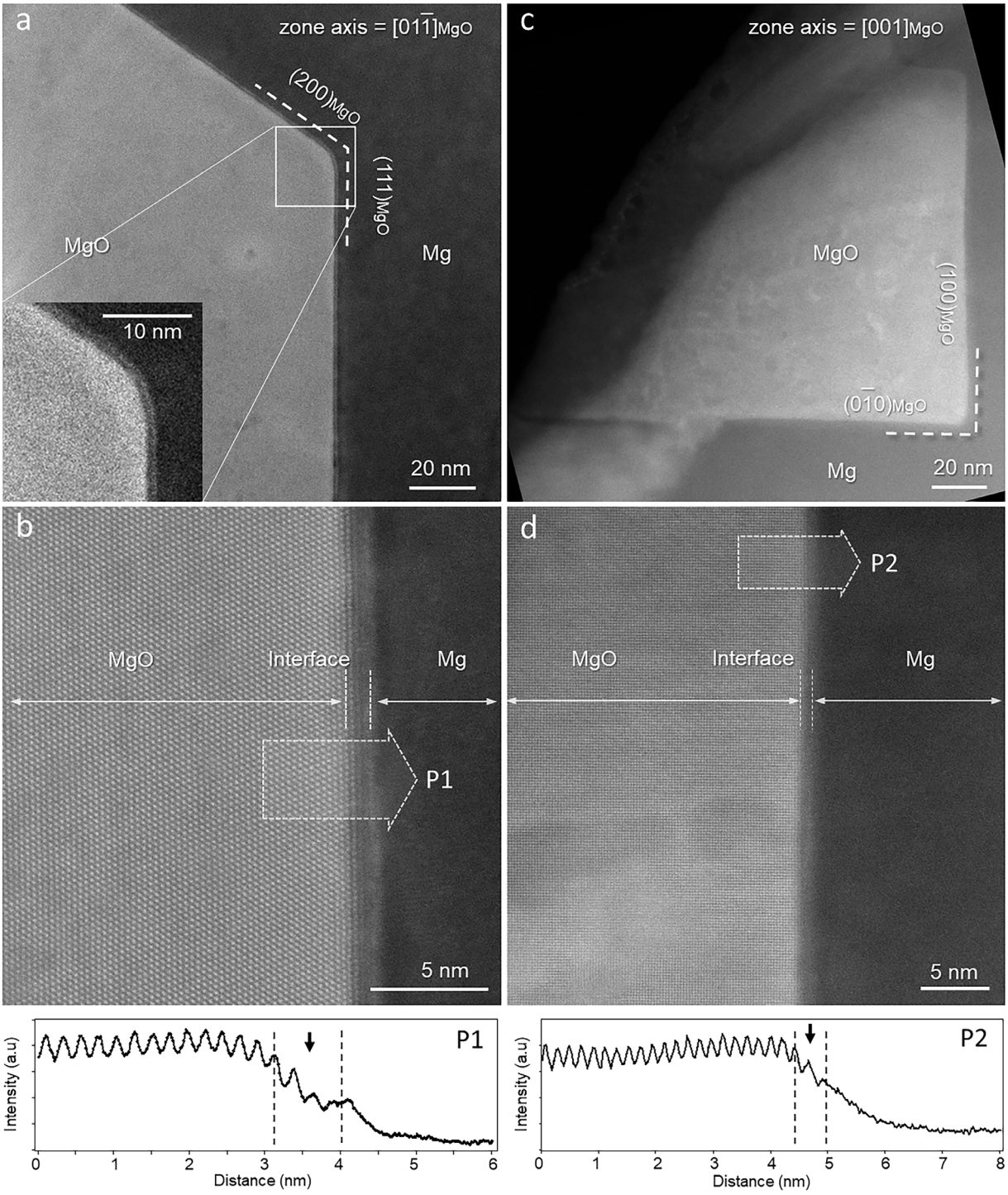

Fig. 8. HAADF STEM images showing the segregation layers decorating both (a, b) octahedral and (c, d) cubic MgO particles at low (a, c) and high (b, d) magnifications. The incident beam is parallel to the $[01\text{-}1]_{MgO}$ zone axis in (a, b), while the zone axis is $[001]_{MgO}$ in (c, d). Inset in (a) magnifies the corner feature marked by the white square. The contrast profiles along 'P1' and 'P2' show that the segregation layers on both particles have a lower contrast intensity than the MgO matrix, with a few atomic layers in thickness.

beam-sensitivity of the interfacial layers make it challenging to obtain an atomically resolved chemical map (we note, for instance, that even the Mg and O columns within the MgO interior, are hardly resolved). However, the spatial distributions of Ca and N, and Mg and O, together with the simultaneously observed HAADF and MAADF contrast, strongly suggest that Ca and N are likely to randomly occupy the Mg and O sites, respectively, resulting in a terminating atomic plane that contains both Mg and Ca atoms. It is however clear that Ca and N solute atoms co-segregate at the $\{111\}_{MgO}$/Mg interface resulting in the formation of interfacial layers rich in Ca and N, poor in Mg and O, which exhibit an atomic struc-

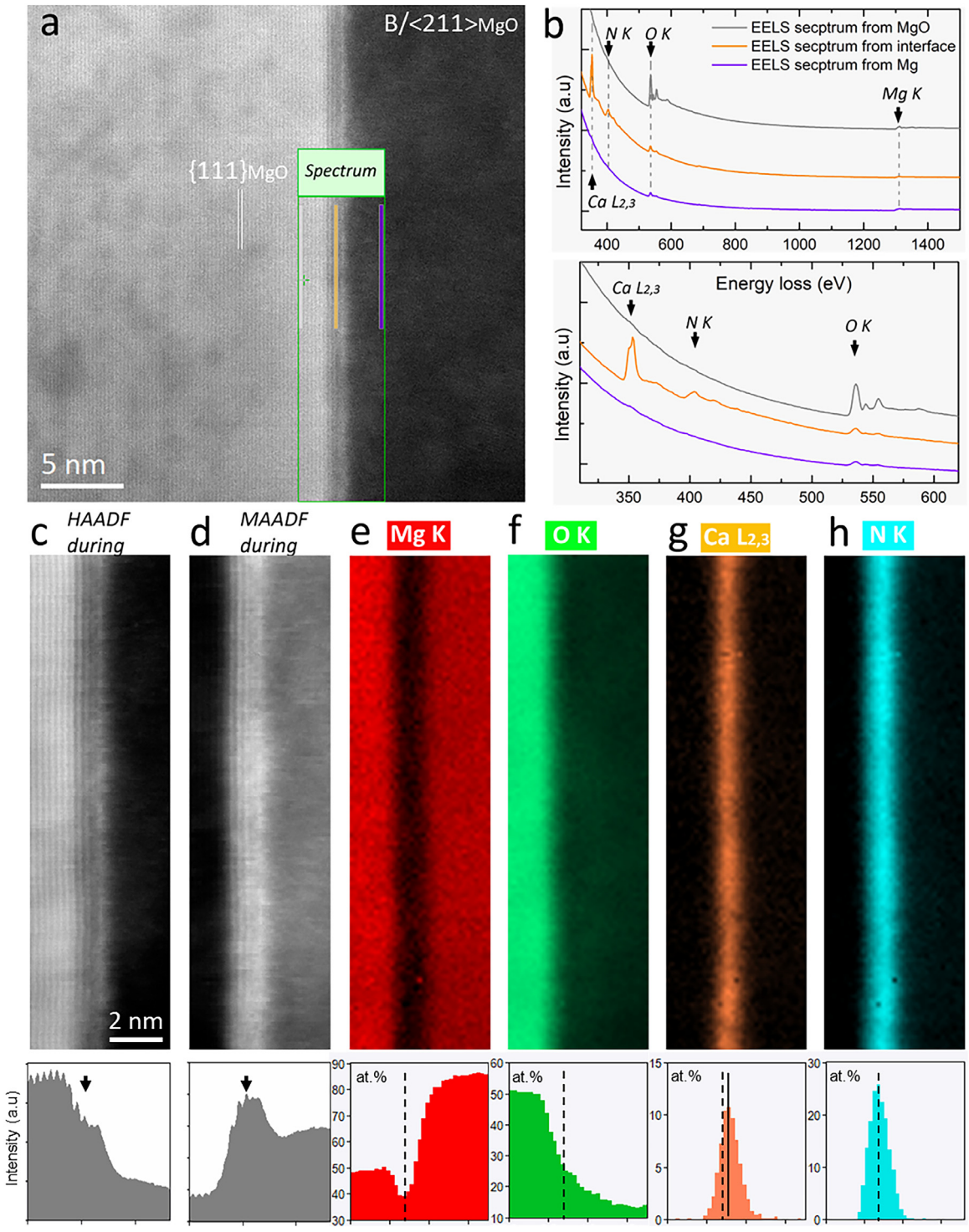

Fig. 9. STEM and EELS analyses at the $\{111\}_{MgO}$/Mg interface suggesting the co-segregation of Ca and N. (a) HAADF STEM image of the interface viewed along $<211>_{MgO}$ direction; (b) EELS core-loss spectra extracted from corresponding areas marked with coloured rectangles in (a); (c, d) HAADF and MAADF images along with the contrast profiles acquired during EELS acquisition; and (e-h) EELS elemental maps of Mg, O, Ca and N, associated with the quantification results. The dashed lines on the chemical profiles mark the corresponding positions of the maxima of the N, while the solid line highlights the Ca maximum; an offset is noticed between the N and Ca maxima.

ture related to but deviating slightly from that of the MgO interior.

Irrespective of the crystallographic terminations, the interfacial layers at the $\{100\}_{MgO}$/Mg interfaces also inherit the atomic structure of parent MgO with atomic deviations, and are compositionally concentrated in Ca and N. Fig. 11 provides further atomic-resolution HAADF STEM images and EELS spectrum image acquired across the $\{100\}_{MgO}$/Mg in-

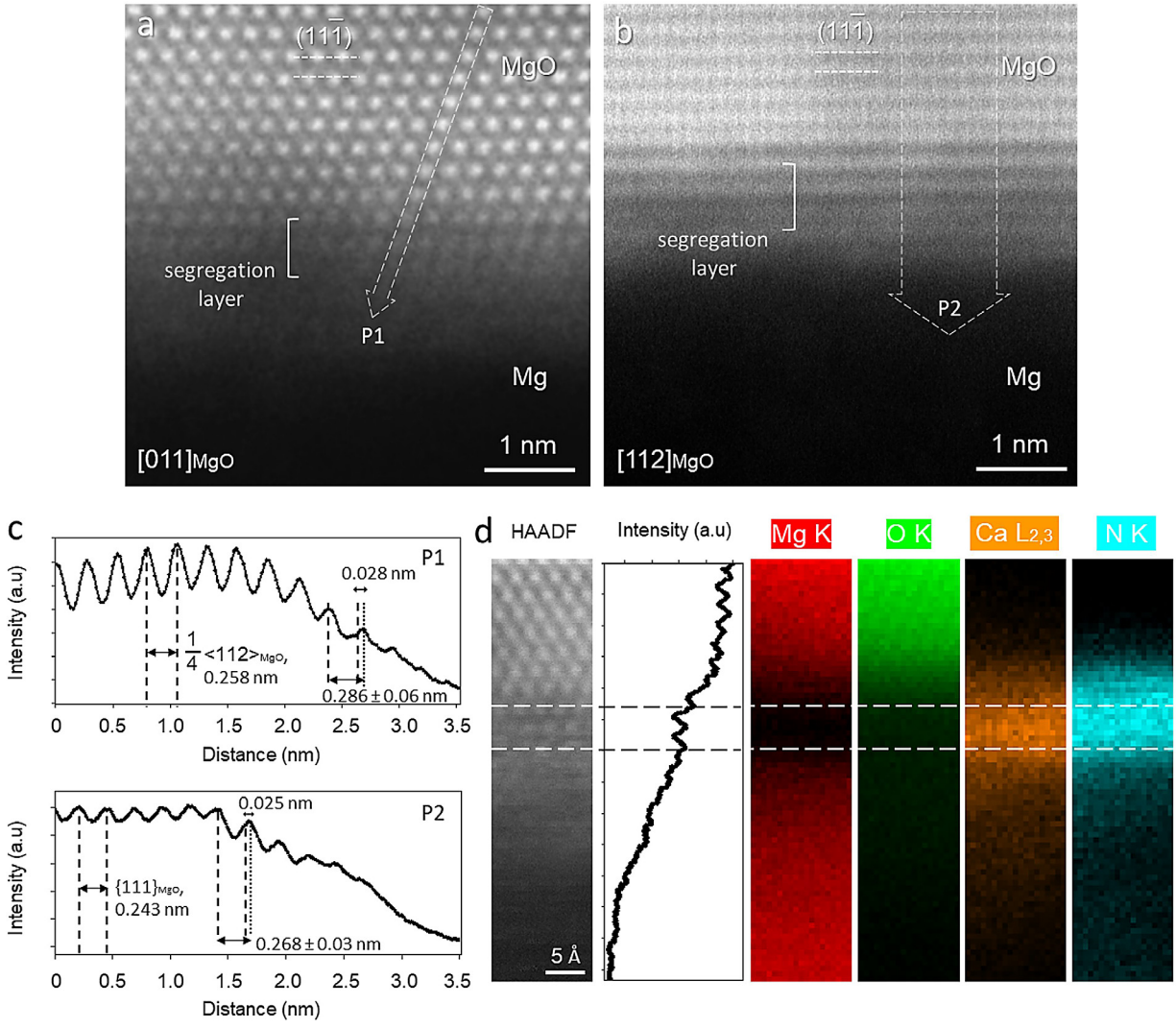

Fig. 10. Atomic structure and composition of the interfacial layers at the $\{111\}_{MgO}$/Mg interface characterised by atomic-resolution HAADF and EELS analysis. (a, b) HAADF STEM images of the $\{111\}_{MgO}$/Mg interfaces viewed along (a) $[011]_{MgO}$ and (b) $[112]_{MgO}$, respectively; (c) contrast profiles along 'P1' in (a) and 'P2' in (b), respectively; (d) HAADF during image and the corresponding EELS elemental maps of Mg, O, Ca and N generated by integrating specific edges with a suitable window over the acquisition area. Ca and N can be seen concentrated at the interface, where the atomic structure is identical as MgO matrix.

terfaces, with the electron beams parallel to either $[001]_{MgO}$ or $[011]_{MgO}$ directions. The contrast variations in Fig. 11a–c confirm that the interfacial layers comprise three to four atomic layers of uniform but lower-intensity contract compared to the MgO matrix, where the atomic-column arrangement follows the MgO pattern but is less distinct ('fuzzy'). The atomic structure of the interfacial layers appears consistent, regardless of the termination facets. In particular, Fig. 11b shows the interfacial layers at the $\{100\}_{MgO}$/Mg interface under the same zone axis of $[011]_{MgO}$ as that in Fig. 10a acquired at the $\{111\}_{MgO}$/Mg interface, both interfacial layers resemble the MgO interior but deviated slightly. An expansion of 0.012 nm is measured for the interfacial layers along the direction normal to the $(200)_{MgO}$ plane ('P1' in Fig. 11a), while the value is 0.018 nm along the $<112>_{MgO}$ direction ('P1' in Fig. 11b), in average accounting for a ~6% expansion of lattice constant. The EELS elemental maps in Fig. 11d, while still noisy, confirm that Ca and N are located on the same atomic planes as within the MgO interior, as both Ca and N maps retain the atomic periodicity of the MgO. However, since in this projection each {100} atomic plane originally contains 50% Mg and 50% O, the distributions of Ca and N cannot be spatially separated.

We have provided an atomic-level observation of both $\{111\}_{MgO}$/Mg and$\{100\}_{MgO}$/Mg interfaces modified by the co-segregations of Ca and N in a Mg-0.5Ca alloy (Figs. 8–11). Combining the above structural and chemical analysis, we therefore conclude that the interfacial layers are chemically deviated from the MgO matrix, while the lattice structure is defective but remains similar to the MgO matrix. This phenomenon is independent of faceted crystal planes of MgO particles.

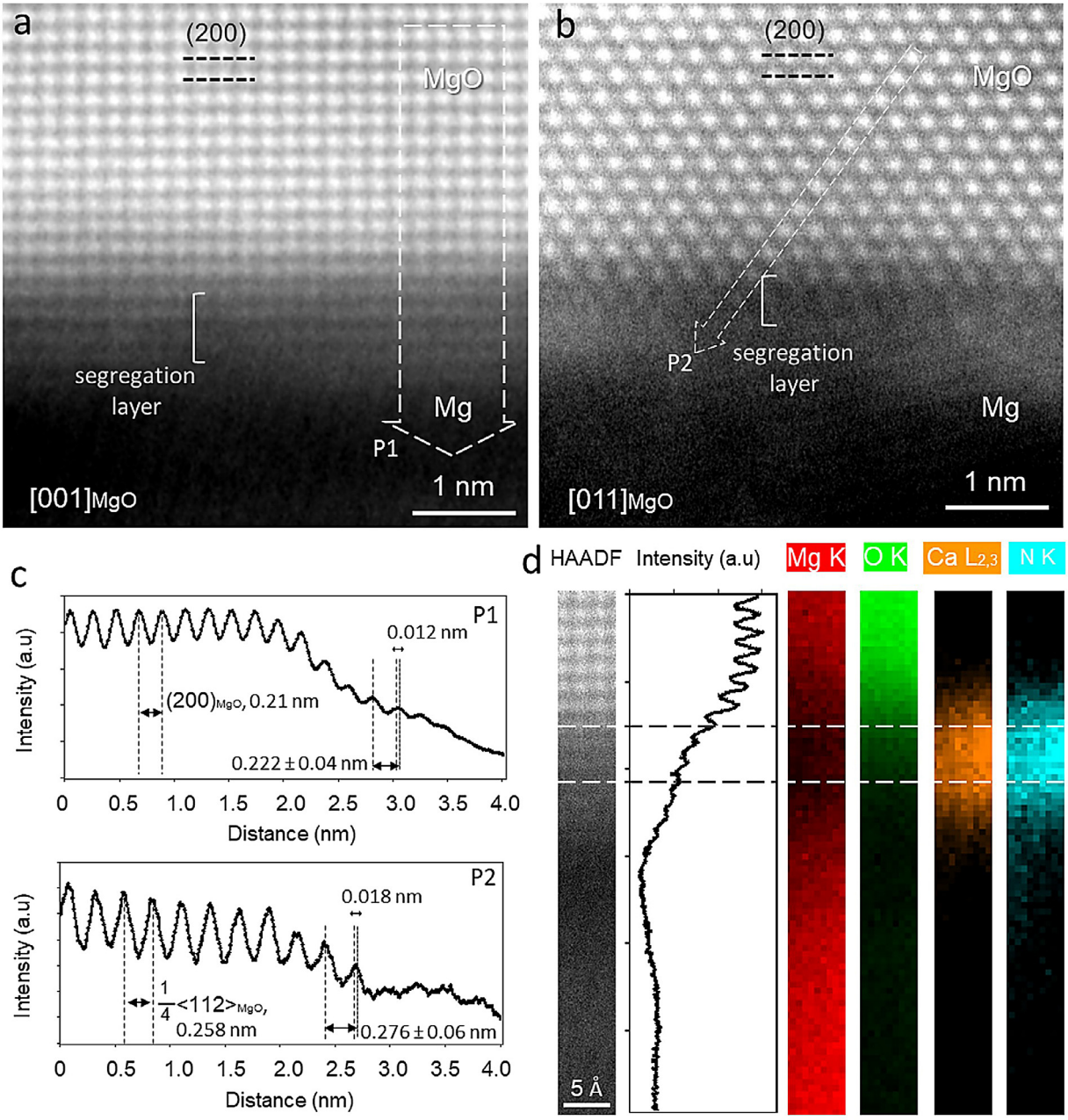

Fig. 11. Atomic structure and composition of the interfacial layers at the $\{100\}_{MgO}$/Mg interface characterised by atomic-resolution HAADF and EELS analysis. (a, b) HAADF STEM images of the $\{100\}_{MgO}$/Mg interfaces viewed along (a) $[001]_{MgO}$ and (b) $[011]_{MgO}$ respectively; (c) contrast profiles along the labelled P1 and P2 in (a) and (b), respectively; (d) HAADF during image and the corresponding EELS elemental maps of Mg, O, Ca and N generated by integrating specific edges with a suitable window over the acquisition area. Ca and N can be seen concentrated at the interface, where the atomic structure is identical as MgO matrix.

4. Discussion

The modification of MgO by Ca or N has been reported before 45,46,55,56]. Using aberration-corrected STEM, Yan *et al.* [46] have observed that Ca can substitute Mg sites at a 24° [001] tilt MgO grain boundary. As simulated by Masri *et al.* [55], Ca can substitutionally dope the $\{100\}_{MgO}$ surface. After surface structural relaxation to a low energy state, Ca doping atoms protrude upward due to the size difference, while the neighbouring Mg and O atomic positions also deviate from their original sites [55]. Density functional theory (DFT) calculation also revealed that N can substitute O atoms in bulk MgO and introduce vacancies [56]. Consistent with these earlier reports, here we also observe that Ca and N respectively substitute Mg and O sites and in a random manner (Figs. 9–11). The observed image intensity further suggests that vacancies may exist as one of the factors decreasing the HAADF image intensity: although N is lighter than O, a fully stoichiometric substitution of Ca for Mg should on first approximation result in a brighter layer than pure MgO. Fur-

thermore, the HAADF contrast can also be affected by static atomic displacement and strain [57,58], both of which disrupt the channelling of the electron probe and so may weaken the image intensity. Overall, and in conjunction with the observations from the EELS chemical maps, the atomic arrangements in the Ca/N co-segregation layers are expected to be less ordered and more defective as compared to the parent MgO substrate.

With a lattice misfit of 7.9% with pure Mg, MgO was long thought of as a poorly potent substrate for nucleating Mg solid [24]. The Ca/N co-segregation layers observed here exhibit a similar lattice structure as the MgO matrix. If the measured lattice expansion is isotropic, the misfit with Mg will be reduced and thus the potency of the Ca/N co-segregation layers may be improved as compared to the parent MgO. However, the observed atomic displacement, in association with chemical changes, is irregular, as illustrated by their fuzzy and lower contrast than the parent MgO matrix (Figs. 10 and 11). It means that the atomic arrangements in the terminating plane of the Ca/N co-segregation layers deviates randomly away from the lattice sites, with components either in parallel with or normal to the termination plane. Both in-plane disordering and atomic surface roughness are therefore introduced, which degrade the nucleating capability of a substrate by poisoning the prenucleation process [59–62]. As proposed in the previous work [59–61], prenucleation occurs at a temperature above the liquidus, whose behaviour is characterised by the ordering of liquid atoms above a template substrate in a range of a few atomic layers. Once the terminating atomic plane becomes atomically rough and/or less ordered to be a poor template, the prenucleation process above will be retarded [59–61]. Additionally, the different chemical interactions of terminating ions with liquid atoms will roughen the prenucleation layers [60]. The subsequent nucleation will be affected since the prenucleation structure provides a precursor at the nucleation temperature for heterogeneous nucleation following a layer-by-layer growth mechanism [63]. As compared to MgO, the atomic-level disordering and different ion species in the Ca/N co-segregation layers make the substrate a poorer structural template, upon which the atomic ordering of liquid Mg atoms will be impeded during prenucleation, therefore impacting the subsequent nucleation process. As a result, Ca/N co-segregation could further deteriorate the potency of MgO, being impotent for nucleating α-Mg .

Nevertheless, grain refinement is enhanced as more dispersed MgO particles are generated in the Mg-xCa melts, either through HSMC or HSO, as demonstrated in Fig. 7. It suggests that the impotent MgO particles, as the predominant inclusions, still act as the nucleation sites and are responsible for the refining mechanism. But the solidification behaviour may vary from that in the system inoculated with highly potent inoculant particles. Fan *et al.* [28] proposed that impeding nucleation can lead to more significant grain refinement through a solidification behaviour dominated by explosive grain initiation (EGI). It is plausible that, under specific circumstances, impotent nucleating particles that require a large nucleation undercooling can be harnessed for grain refinement. A numerical model of this solidification behaviour was successfully applied to the representative system of Mg alloys containing nanosized MgO particles of a large number density and a narrow size distribution [28]. Since the fixed nucleation undercooling (ΔT_n) is larger than the size-related grain initiation undercooling (ΔT_{gi}) for most of MgO particles due to the poor potency, upon solidification the melt was cooled until the thermal undercooling (ΔT_{th}) triggers simultaneously nucleation and grain initiation on a large amount of MgO substrates that satisfy both nucleation and grain initiation criteria: $\Delta T_{gi} \leq \Delta T_n = \Delta T_{th}$. Such grain initiation events occur explosively and release huge latent heat in a short time and may lead to an immediate recalescence. This is different from the grain initiation events occurring on highly potent substrates. Initially, nucleation occurs on all available particles that satisfy $\Delta T_n = \Delta T_{th}$. Due to curvature constrain, which is inversely proportional to the substrate size, grain initiation occurs firstly on the largest particle as the melt temperature drops and ΔT_{th} increases, then it occurs progressively on smaller ones until recalescence [4,28]. Such a behaviour is called progressive grain initiation (PGI).

The proposed grain initiation and grain refinement maps in Ref. [28] can be applied to understand the solidification behaviour in the samples of Mg-xCa, Mg-xCa-HSMC, and Mg-xCa-HSO, in which the key differences are the number density of MgO and Ca content (*i.e.*, growth restriction).

In the Mg-xCa melts, MgO particles agglomerate as oxide films, in which most particles around the nucleation site are redundant due to the solute-partitioning-caused grain initiation free zone, resulting in a marked decrease in the effective number density. The grain initiation pattern shifts into a PGI-dominant zone when the particle number density decreases or if the growth restriction increases. Specifically, when the melt is cooled down and thermal undercooling reaches ΔT_n, the number of EGI events on impotent MgO particles is too low to cause recalescence in the initial stage. Afterwards, the melt keeps cooling to trigger more grain initiations progressively on smaller MgO particles in a PGI manner. As the Ca content increases, latent heat is impeded by sufficient growth restriction to allow more PGI events, and the grain size decreases. As a result, the Mg-xCa melts solidify in a PGI-dominant pattern. However, the small number density of MgO particles in dispersion has limited the grain refinement performance.

When HSMC or HSO is applied, the particle number density of MgO particles increases dramatically due to the dispersion of MgO films, which pulls the grain initiation mechanism into the EGI-dominant region [28]: more MgO particles (which satisfy $\Delta T_{gi} \leq \Delta T_n$) participate in nucleation and grain initiation instantaneously (*i.e.,* EGI) when ΔT_{th} reaches ΔT_n. At this stage, it would appear that the higher number of dispersed MgO particles leads to more EGI events, and therefore to a smaller grain size. Spontaneously, the solid growth on these EGI sites generates a huge latent heat, which may cause immediate recalescence depending on the alloy composition (growth restrictions) and cooling condition. On this basis, growth restriction can reduce the EGI proportion by generating additional PGI events afterward if it is strong enough

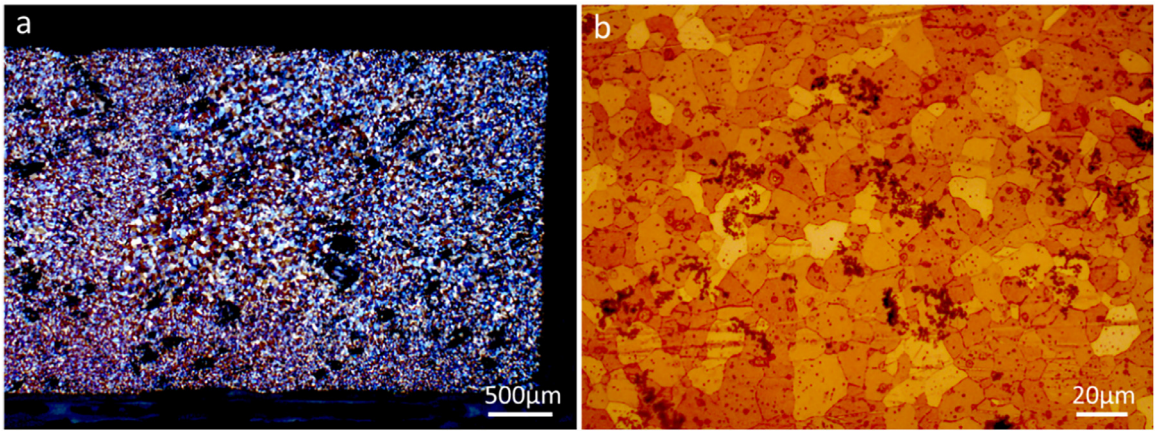

Fig. 12. Optical micrographs showing the grain structures of Mg-0.5Ca-HSO prepared by vaccum suction casting into a 3 mm Cu cylinder mould, where a cooling rate within 10^2–10^3 K/s is expected.

to delay recalescence. That is to say, the increasing growth restriction can shift grain initiation pattern towards the PGI side, while move grain size to a smaller value in the grain refinement map [28]. This mechanism suggests that the increasing Ca content can delay recalescence to some extent, allowing additional PGI events on smaller MgO particles to further refine the grain structure, as seen in Figs. 3 and 6. Whereas the effect of Ca is very limited in Mg-xCa-HSO, which generates the most latent heat during EGI among the three sets. Together with the cube-root relationship between grain initiation events and grain size, they explain why the plot of Mg-xCa-HSO in Fig. 7 has the smallest slope.

As the predominant type of native MgO, {111} MgO particles in both Mg-0.5Ca and Mg-0.5Ca-HSO possess a log-normal distribution. As shown in Fig. S7, the HSO treatment causes particle coarsening, slightly shifting the fitted curve to the right. The mean average size increases from 70 nm to 83 nm, while the standard deviation from 0.34 to 0.39. Given a certain number density of MgO, this shift is expected to allow more particles falling in the size ranges satisfying both nucleation and grain initiation criteria, thus promote EGI for a finer grain size. Therefore, the changed size distribution could be another factor for finer grain size in the Mg-xCa-HSO series.

There may exist other nucleant particles/sites of higher potency than MgO in the melt. For instance, MgS has a 0.92% lattice misfit with Mg at room temperature along the atomic directions in the close-packed atomic plane: $<112>_{MgS}//<11\text{-}20>_{Mg}$. A system that solidifies in an EGI-dominant manner will be sensitive to their existence. Due to nucleation competition, nucleation and grain initiation occurs firstly on these particles that satisfy $\Delta T_n < \Delta T_{gi} = \Delta T_{th}$ in a PGI manner. The competing particles in the test samples of this work have an extremely small number density, as particle types other than MgO were rarely observed. Nonetheless, their likely existence and the absence of sufficient growth restriction will result in fast growth of columnar grains that quickly cause recalescence, stopping any impotent MgO particles from participating in an EGI manner. Therefore, the growth restriction, *i.e.*, the addition of Ca in this case, becomes critical to impede grain growth, to delay recalescence, and to increase thermal undercooling ΔT_{th} for further nucleation and grain initiation on the impotent MgO particles in a EGI manner. Therefore, the more Ca is added, the larger the tolerance of the system becomes.

In contrast to the growth restriction effect limited by the solute content, the cooling rate has a much larger manipulable range to delay thermal recalescence, which is expected to activate more MgO particles for grain refinement in a PGI manner. To test this hypothesis, we remelted the Mg-0.5Ca-HSO and applied a vacuum suction casting method that achieves a cooling rate in the range of 10^2–10^3 K/s. Native MgO shows a great potential for grain refinement in Mg-Ca alloys. As depicted in Fig. 12, the obtained grain size is 11.8 ± 0.5 μm, which is much smaller than the counterpart cooled at 3.5 K/s (76.9 ± 2.2 μm). This suggests that over two orders of magnitude more MgO particles, which use to be abundant at a cooling rate of 3.5 K/s, are triggered to contribute to further grain size reduction.

As elucidated above, the most critical part of the mechanism is to boost native and impotent MgO particle for explosive grain initiation. The native MgO films/particles, the addition of Ca, and the application of HSMC work collaboratively at achieving grain refinement in Mg-Ca alloys. The HSMC treatment enables the dispersion of native MgO particles, which can be facilitated if the interfacial energy can be reduced when Ca is added for interfacial segregation. At the same time, by promoting mass transport, HSMC is essential to promote interfacial segregation that further poisons the nucleation potency of MgO particles. As a result, the EGI events' number and proportion increase as the particle number density increases, leading to a finer grain size. Although more Ca content (growth restrictions) or larger cooling rate can raise further PGI events afterwards to lower the EGI proportion, the absolute number of grain initiation events increases to result in a finer grain size.

5. Conclusions

1. The grain refinement of Mg-Ca alloys is enhanced by the addition of Ca, the application of high shear melting conditioning (HSMC) or HSMC with additional melt oxidation (HSO).
2. As the predominant inclusion, native MgO particles act as the substrates for heterogeneous nucleation of α-Mg grains.
3. The addition of Ca modifies native MgO particles along with N through interfacial segregation on both the {111} and {100} crystal facets, while leaving the particle size and morphology unaffected.
4. The Ca and N co-segregation layers structurally resemble the lattice structure of MgO matrix, with Ca and N occupying the Mg and O sites, respectively, causing lattice expansion and local atomic displacements. This renders the potency inferior to the parent MgO.
5. With the growth restriction and interfacial segregation caused by Ca additions, the modified MgO particles of a large number density after HSMC or HSO can be harnessed for more significant grain refinement in Mg-Ca alloys through an explosive grain initiation (EGI) dominant solidification process.

Declaration of competing interest

The authors declare that they have no known competing financial interests or personal relationships that could have appeared to influence the work reported in this paper.

CRediT authorship contribution statement

Shihao Wang: Writing – review & editing, Writing – original draft, Validation, Methodology, Investigation, Formal analysis, Data curation. **Yun Wang:** Writing – review & editing, Supervision. **Quentin M. Ramasse:** Writing – review & editing, Supervision, Methodology, Investigation, Data curation. **Zhongyun Fan:** Writing – review & editing, Supervision, Resources, Project administration, Funding acquisition, Conceptualization.

Acknowledgements

EPSRC is gratefully acknowledged for financial support under grant number EP/N007638/1. The SuperSTEM Laboratory is the UK National Research Facility for Advanced Electron Microscopy, supported by EPSRC under grant number EP/W021080/1. SHW gratefully acknowledges ETC in Brunel University for providing access to the facilities. The authors would like to gratefully acknowledge Dr. Feng Wang, Dr. Feng Gao, Mr. Peter Lloyd, Dr. Yijie Zhang, Dr. Chamini Mendis, and Dr. Qing Cai for their assistance in casting experiments and inspiring discussion. SHW would like to thank Dr. Eric Prestat at SuperSTEM Laboratory for his assistance and expertise during the characterisation sessions.

Supplementary materials

Supplementary material associated with this article can be found, in the online version, at doi:10.1016/j.jma.2024.03.009.

References

[1] A.A. Luo, J. Magnes. Alloy. 1 (2013) 2–22.
[2] N. Li, Y. Zheng, J. Mater. Sci. Technol. 29 (2013) 489–502.
[3] M. Alderman, A. Perspective, in: Magnesium Technology, 2016, Springer, Cham, 2016, pp. 59–60.
[4] A.L. Greer, A.M. Bunn, A. Tronche, P.V. Evans, D.J. Bristow, Acta Mater. 48 (2000) 2823–2835.
[5] D.H. StJohn, M. Qian, M.A. Easton, P. Cao, Z. Hildebrand, Metall. Mater. Trans. A. 36A (2005) 1669–1679.
[6] D.H. Stjohn, M.A. Easton, M. Qian, J.A. Taylor, Metall. Mater. Trans. A. 44 (2013) 2935–2949.
[7] J. Lelito, P.L. Zak, A.A. Shirzadi, A.L. Greer, W.K. Krajewski, J.S. Suchy, K. Haberl, P. Schumacher, Acta Mater. 60 (2012) 2950–2958.
[8] D.H. Stjohn, M. Qian, M.A. Easton, P. Cao, Acta Mater. 59 (2011) 4907–4921.
[9] X. Gao, S.M. Zhu, B.C. Muddle, J.F. Nie, Scr. Mater. 53 (2005) 1321–1326.
[10] B.S. You, W.W. Park, I.S. Chung, Scr. Mater. 42 (2000) 1089–1094.
[11] Y.C. Lee, A.K. Dahle, D.H. StJohn, Metall. Mater. Trans. A 31 (2000) 2895–2906.
[12] Z. Li, X. Gu, S. Lou, Y. Zheng, Biomaterials 29 (2008) 1329–1344.
[13] S.H. Ha, J.K. Lee, H.H. Jo, S. Jung, S.K. Kim, Rare Met. 25 (2006) 150–154.
[14] S.H. Ha, J.K. Lee, S.K. Kim, Mater. Trans. 49 (2008) 1081–1083.
[15] Y.C. Gu, G.S. Peng, G.S. Song, J. Huang, Y. Wang, S.Y. Chen, Int. J. Cast Met. Res. 32 (2019) 295–303.
[16] J. Jeong, J. Im, K. Song, M. Kwon, S. Kwang, Acta Mater. 61 (2013) 3267–3277.
[17] B. Wiese, C.L. Mendis, D. Tolnai, A. Stark, N. Schell, H.P. Reichel, R. Brückner, K.U. Kainer, N. Hort, J. Alloys Compd. 618 (2015) 64–66.
[18] Y. Ali, D. Qiu, B. Jiang, F. Pan, M.X. Zhang, Scr. Mater. 114 (2016) 103–107.
[19] G.S. Peng, G.S. Song, Y. Wang, K.H. Chen, S.Y. Chen, Int. J. Cast Met. Res. 31 (2018) 99–107.
[20] S.H. Wang, F. Wang, Y. Wang, Q.M. Ramasse, Z. Fan, IOP Conf. Ser. Mater. Sci. Eng. 529 (2019) 012048.
[21] H. Hall, Magnes. Rev. 3 (1945) 68 Abs..
[22] Z. Fan, Y. Wang, M. Xia, S. Arumuganathar, Acta Mater. 57 (2009) 4891–4901.
[23] H. Men, B. Jiang, Z. Fan, Acta Mater. 58 (2010) 6526–6534.
[24] S. Wang, Y. Wang, Q. Ramasse, Z. Fan, Metall. Mater. Trans. A 51 (2020) 2957–2974.
[25] H. Liao, L. Mo, X. Zhou, B. Zhao, J. Du, J. Mater. Res. Technol. 12 (2021) 807–817.
[26] L. Rogal, L. Litynska-Dobrzynska, Mater. Sci. Technol. 35 (2019) 349–360 (United Kingdom).
[27] Z. Fan, M. Xia, H. Zhang, G. Liu, J.B. Patel, Z. Bian, I. Bayandorian, Y. Wang, H.T. Li, G.M. Scamans, Int. J. Cast Met. Res. 22 (2009) 103–107.
[28] Z. Fan, F. Gao, B. Jiang, Z. Que, Sci. Rep. 10 (2020) 1–11.
[29] G. Lin, D. Liu, M. Chen, C. You, Z. Li, Y. Wang, W. Li, Mater. Charact. 144 (2018) 120–130.
[30] Z. Ma, C. Li, J. Du, M. Zhan, Int. J. Met. 13 (2019) 674–685.
[31] B. Jiang, W. Liu, D. Qiu, M.X. Zhang, F. Pan, Mater. Chem. Phys. 133 (2012) 611–616.
[32] D. Qiu, M.X. Zhang, J.A. Taylor, P.M. Kelly, Acta Mater. 57 (2009) 3052–3059.
[33] L. Lu, A.K. Dahle, D.H. Stjohn, Scr. Mater. 53 (2005) 517–522.
[34] D. Qiu, M.X. Zhang, J. Alloys Compd. 586 (2014) 39–44.

[35] S. Wang, PhD Thesis, Brunel University, 2020.
[36] C. Barth, C.R. Henry, Phys. Rev. Lett. 91 (2003) 196102/1-196102/4.
[37] P. Cao, M. Qian, D.H. StJohn, Scr. Mater. 56 (2007) 633–636.
[38] Z. Fan, Y. Wang, Y. Zhang, T. Qin, X.R. Zhou, G.E. Thompson, T. Pennycook, T. Hashimoto, Acta Mater. 84 (2015) 292–304.
[39] Z. Fan, Metall. Mater. Trans. A 44 (2013) 1409–1418.
[40] P. Schumacher, A.L. Greer, Mater. Sci. Eng. A 178 (1994) 309–313.
[41] Y. Wang, C.M. Fang, L. Zhou, T. Hashimoto, X. Zhou, Q.M. Ramasse, Z. Fan, Acta Mater. 164 (2019) 428–439.
[42] Y. Wang, Z. Que, T. Hashimoto, X. Zhou, Z. Fan, Metall. Mater. Trans. A 51 (2020) 5743–5757.
[43] Y. Li, B. Hu, B. Liu, A. Nie, Q. Gu, J. Wang, Q. Li, Acta Mater. 187 (2020) 51–65.
[44] Z. Fan, F. Gao, Y. Wang, H. Men, L. Zhou, Prog. Mater. Sci. 123 (2022) 100809.
[45] R.C. McCune, P. Wynblatt, J. Am. Ceram. Soc. 66 (1983) 111–117.
[46] Y. Yan, M.F. Chisholm, S.J. Pennycook, S.T. Pantelides, Surf. Sci. 442 (1999) 251–255.
[47] G.S. Peng, Y.C. Gu, G.S. Song, Y. Wang, S.Y. Chen, Int. J. Cast Met. Res. 34 (2021) 6–13.
[48] M. Watanabe, M. Kanno, D. Ackland, C. Kiely, D. Williams, Microsc. Microanal. 13 (2007) 2006–2007.
[49] X. Yang, Y. Huang, N.S. Barekar, S. Das, I.C. Stone, Z. Fan, Compos. Part A 90 (2016) 349–358.
[50] J.B. Patel, X. Yang, C.L. Mendis, Z. Fan, JOM 69 (2017) 1071–1076.
[51] S. Lun Sin, A. Elsayed, C. Ravindran, Int. Mater. Rev. 58 (2013) 419–436.
[52] H.J.T. Ellingham, J. Soc. Chem. Ind. 63 (1944) 125–160.
[53] R.F. Egerton, Electron Energy-Loss Spectroscopy in the Electron Microscope, Springer Science & Business Media, 2011.
[54] P.J. Phillips, M. De Graef, L. Kovarik, A. Agrawal, W. Windl, M.J. Mills, Ultramicroscopy 116 (2012) 47–55.
[55] P. Masri, P.W. Tasker, Surf. Sci. 149 (1985) 209–225.
[56] M. Pesci, F. Gallino, C. Di Valentin, G. Pacchioni, J. Phys. Chem. C 114 (2010) 1350–1356.
[57] V. Grillo, E. Carlino, F. Glas, Phys. Rev. B Condens. Matter Mater. Phys. 77 (2008) 1–6.
[58] Z. Yu, D.A. Muller, J. Silcox, J. Appl. Phys. 95 (2004) 3362–3371.
[59] B. Jiang, H. Men, Z. Fan, Comput. Mater. Sci. 153 (2018) 73–81.
[60] C.M. Fang, Z. Fan, Metall. Mater. Trans. A 51 (2020) 788–797.
[61] H. Men, Z. Fan, Metall. Mater. Trans. A 49 (2018) 2766–2777.
[62] H. Men, C. Fang and Z. Fan, *Metals*, **12 (10)**, 2022, 1704-1734.
[63] Z. Fan, H. Men, Mater. Res. Express 7(12) (2020) 126501-14.